these alloys, relative to the overall trend. The activity loss also correlates with the thickness of the overlayer (Fig. 3E) (3). Our density functional theory (DFT) calculations on the stability of different Pt overlayers, expressed as dissolution potential, show that the stability decreases as the compressive strain increases (Fig. 3F)—i.e., strain is a stability descriptor. We attribute the apparent thickening of the Pt overlayer with cycling to surface diffusion processes (28); bulk diffusion of lanthanide atoms through the overlayer will be strongly impeded by the strength of E_a (13). The strain-induced destabilization of the Pt overlayer could facilitate surface mobility (28), providing a channel for the dissolution of any residual lanthanide atoms in close vicinity to the surface. In summary, Fig. 3, D to F, shows that the overlayer thickness, activity losses, and thermodynamic stability are all a function of the bulk lattice parameter: Increased strain destabilizes the Pt overlayer and thus accelerates surface diffusion.

Figure 4A is a plot of the ORR activity as a function of the lattice parameter, a and d_{Pt-Pt}. Notably, all nine compounds, including the Pt-lanthanides and Pt$_5$Ca, follow the same volcano-type trend, with Pt$_5$Gd and Pt$_5$Tb at the apex. Because ΔE_{OH} is likely correlated with d_{Pt-Pt} (3), the most trivial explanation for this trend is that the plot represents a Sabatier volcano: Alloys on the left bind OH too weakly, whereas on the right hand they bind ΔE_{OH} too strongly (as described by the DFT calculations in figs. S17 and S18). Alternatively, beyond a certain level of bulk strain, the overlayer could be unstable, causing the d_{Pt-Pt} of the overlayer to relax toward a much lower level of surface strain. On single crystals, the destabilization is manifested as a positive shift in the "reversible" voltammetric peak for OH adsorption (1, 10); however, we do not observe this shift on our polycrystalline materials, presumably because of hysteresis (electrochemical "irreversibility") or possibly coadsorption of OH and O. Conversely, the lanthanide contraction results in a clear voltammetric shift for the H adsorption region (figs. S3 and S4), plotted on Fig. 4B, which resembles the activity volcano, with Pt$_5$Tb exhibiting the maximum destabilization of adsorbed H. Notably, we also observe a linear relation between the experimental activity and the potential shift in the H adsorption (fig. S7).

Our DFT calculations on strain-activity-reactivity relations (section S5.4) suggest that Pt$_5$Tb, which is the most active electrocatalyst, should exhibit ~3% compression, approaching the optimum OH binding energy of the Sabatier volcano (11). By comparing our activity data and the voltammetric shift in H adsorption to the DFT predictions, we can conjecture that Pt-lanthanide alloys with a shorter d_{Pt-Pt} than Pt$_5$Tb form a more relaxed overlayer (figs. S19 to S21). More generally, our observations suggest that strain effects can only weaken the binding of H and OH to a certain extent. More appreciable destabilization of reaction intermediates can be afforded by ligand effects (1, 10). The implementation of these catalysts in fuel cells will require scalable synthesis methods yielding high surface catalysts. Nonetheless, we have already demonstrated that Pt$_x$Gd NPs exhibited an outstanding activity of 3.6 Å/mg Pt at 0.9 V RHE in liquid half cells (18, 29) (fig. S6B), only surpassed by Pt$_3$Ni nanoframes (21) and Mo-doped Pt$_3$Ni nanoparticles (22). Careful tuning of the NP composition—for instance, by synthesizing ternary Pt-Gd-Tb alloys, in combination with a judicious choice of annealing treatment (21, 22, 30)—could yield record-breaking catalytic activity and stability over the long term in real devices.

REFERENCES AND NOTES

1. V. R. Stamenkovic et al., Science 315, 493–497 (2007).
2. H. A. Gasteiger, S. S. Kocha, B. Sompalli, F. T. Wagner, Appl. Catal. B 56, 9–35 (2005).
3. P. Strasser et al., Nat. Chem. 2, 454–460 (2010).
4. S. Mukerjee, S. Srinivasan, M. P. Soriaga, J. McBreen, J. Electrochem. Soc. 142, 1409–1422 (1995).
5. B. Han et al., Energy Environ. Sci. 8, 258–266 (2015).
6. I. E. L. Stephens, A. S. Bondarenko, U. Grønbjerg, J. Rossmeisl, I. Chorkendorff, Energy Environ. Sci. 5, 6744 (2012).
7. J. K. Nørskov et al., J. Phys. Chem. B 108, 17886–17892 (2004).
8. F. Calle-Vallejo et al., Science 350, 185–189 (2015).
9. J. Suntivich, K. J. May, H. A. Gasteiger, J. B. Goodenough, Y. Shao-Horn, Science 334, 1383–1385 (2011).
10. I. E. L. Stephens et al., J. Am. Chem. Soc. 133, 5485–5491 (2011).
11. J. Greeley et al., Nat. Chem. 1, 552–556 (2009).
12. V. R. Stamenkovic, B. S. Mun, K. J. J. Mayrhofer, P. N. Ross, N. M. Markovic, J. Am. Chem. Soc. 128, 8813–8819 (2006).
13. U. G. Vej-Hansen, J. Rossmeisl, I. E. L. Stephens, J. Schiøtz, Phys. Chem. Chem. Phys. 18, 3302–3307 (2016).
14. L. Tang et al., J. Am. Chem. Soc. 132, 596–600 (2010).
15. E. F. Holby, W. Sheng, Y. Shao-Horn, D. Morgan, Energy Environ. Sci. 2, 865–871 (2009).
16. M. Escudero-Escribano et al., J. Am. Chem. Soc. 134, 16476–16479 (2012).
17. P. Hernandez-Fernandez et al., Nat. Chem. 6, 732–738 (2014).
18. A. Velázquez-Palenzuela et al., J. Catal. 328, 297–307 (2015).
19. K. J. J. Mayrhofer, K. Hartl, V. Juhart, M. Arenz, J. Am. Chem. Soc. 131, 16348–16349 (2009).
20. L. Dubau et al., Appl. Catal. B 142–143, 801–808 (2013).
21. C. Chen et al., Science 343, 1339–1343 (2014).
22. X. Huang et al., Science 348, 1230–1234 (2015).
23. M. Mavrikakis, B. Hammer, J. K. Nørskov, Phys. Rev. Lett. 81, 2819–2822 (1998).
24. V. Stamenkovic et al., Angew. Chem. Int. Ed. 45, 2897–2901 (2006).
25. V. Ohm et al., J. Alloy. C 238, 95–101 (1996).
26. L. J. Wan, T. Moriyama, M. Ito, H. Uchida, M. Watanabe, Chem. Commun. 2002, 58–59 (2002).
27. L. Vitos, A. V. Ruban, H. L. Skriver, J. Kollar, Surf. Sci. 411, 186–202 (1998).
28. J. Erlebacher, D. Margetis, Phys. Rev. Lett. 112, 155505 (2014).
29. C. M. Pedersen et al., Electrochim. Acta 179, 647–657 (2015).
30. D. Wang et al., Nat. Mater. 12, 81–87 (2013).
31. B. Cordero et al., Dalton Trans. 2008, 2832–2838 (2008).

ICE SHEETS

Antarctic Ice Sheet variability across the Eocene-Oligocene boundary climate transition

Simone Galeotti,[1]* Robert DeConto,[2] Timothy Naish,[3,4] Paolo Stocchi,[5] Fabio Florindo,[6] Mark Pagani,[7] Peter Barrett,[3] Steven M. Bohaty,[8] Luca Lanci,[1] David Pollard,[9] Sonia Sandroni,[10] Franco M. Talarico,[10,11] James C. Zachos[12]

About 34 million years ago, Earth's climate cooled and an ice sheet formed on Antarctica as atmospheric carbon dioxide (CO_2) fell below ~750 parts per million (ppm). Sedimentary cycles from a drill core in the western Ross Sea provide direct evidence of orbitally controlled glacial cycles between 34 million and 31 million years ago. Initially, under atmospheric CO_2 levels of ≥600 ppm, a smaller Antarctic Ice Sheet (AIS), restricted to the terrestrial continent, was highly responsive to local insolation forcing. A more stable, continental-scale ice sheet calving at the coastline did not form until ~32.8 million years ago, coincident with the earliest time that atmospheric CO_2 levels fell below ~600 ppm. Our results provide insight into the potential of the AIS for threshold behavior and have implications for its sensitivity to atmospheric CO_2 concentrations above present-day levels.

The establishment of the Antarctic Ice Sheet (AIS) is associated with an approximate +1.5 per mil increase in deep-water marine oxygen isotopic ($\delta^{18}O$) values beginning at ~34 million years ago (Ma) and peaking at ~33.6 Ma (1–3), with two positive $\delta^{18}O$ steps separated by ~200,000 years. The first positive isotopic step primarily reflects a temperature decrease (4); the second isotopic step has been interpreted as the onset of a prolonged interval of

maximum ice extent [Earliest Oligocene Glacial Maximum (EOGM)] between 33.6 and 33.2 Ma (5). Deep-water temperature cooled by 3° to 5°C (6) as a consequence of decreasing CO_2 levels (7), while the volume of ice on Antarctica expanded to either near-modern dimensions (6, 8) or as much as 25% larger than present-day values (9,10). A sea-level fall of ~70 m is estimated from low-latitude shallow-marine sequences (9, 11). Uncertainties in the magnitudes of these estimates in part reflect the limitations of geochemical proxy records used to deconvolve the relative contribution of ice volume and temperature at orbital resolution (12), as well as uncertainties inherent in the backstripping of continental margin sedimentary records (8). Ice sheet–proximal marine geological records from the continental margin of Antarctica can improve our understanding of the AIS evolution by providing evidence of the direct response of shallow-marine sedimentary environments (e.g., water depth changes) to ice sheet expansion and retreat.
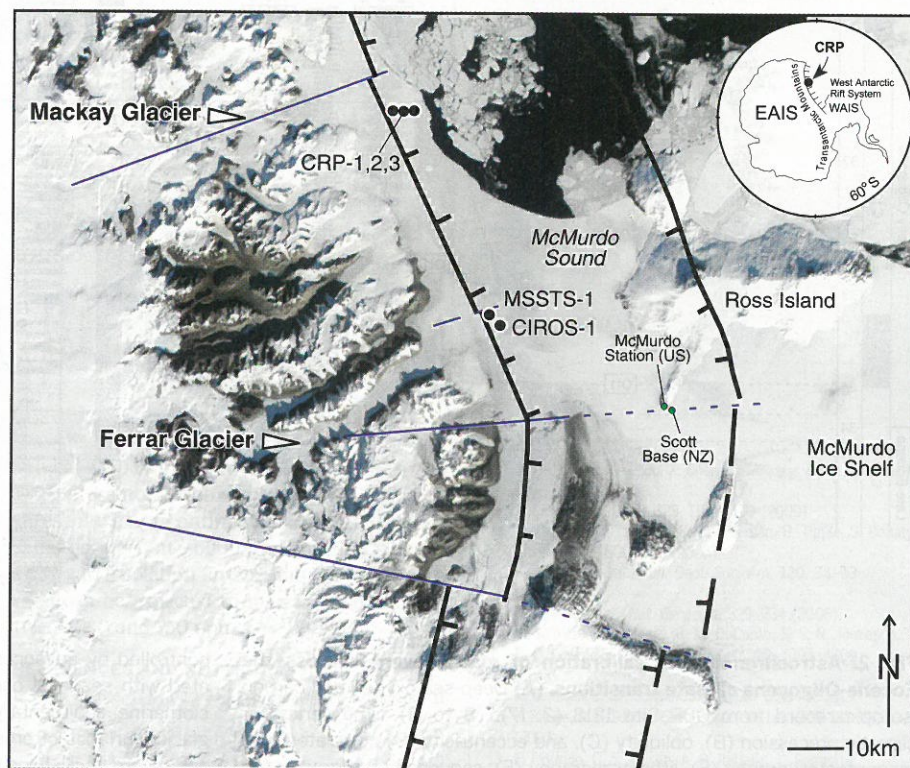
The temporal pattern and extent of Late Eocene–Early Oligocene (~34.1 to ~31 Ma) Antarctic glacial advance and retreat is recorded in the well-dated CRP-3 drillcore, a shallow-water glaciomarine sedimentary succession deposited in the Victoria Land Basin (Fig. 1), tens of kilometers seaward of the present-day East Antarctic Ice Sheet (EAIS) in the Western Ross Sea (13). Thirty-seven fluvial to shallow-marine (deltaic) sedimentary cycles occur in the lower 500 m of the drillcore [330 to 780 m below sea floor (mbsf)] that record the advance and retreat of land-terminating glaciers delivering terrigenous sediment to an open wave–dominated coastline and are associated with relative sea level (RSL) oscillations of less than 20 m (14). These cycles, characterized as type B (Fig. 2; see also supplementary materials), do not display evidence of ice contact from glacial overriding. In contrast, 11 glacio-marine sedimentary cycles bounded by glacial surfaces of erosion in the upper 300 m of the drillcore (0 to 300 mbsf) reflect oscillations of the seaward extent of a marine-terminating ice sheet onto the Ross Sea continental shelf and across the CRP-3 drill site associated with larger RSL fluctuations of >20 m (14) (type A cycles in Fig. 2; see also supplementary materials). Tempo-

ral variations in lithofacies, grain size, and clast abundance primarily reflect oscillations in depositional energy that were controlled by changes in water depth and/or glacial proximity (14, 15). Shallow-marine sedimentary cycles analogous to those observed in the CRP-3 drillcore have been directly linked with orbitally driven climatic cycles of the AIS across the Oligocene-Miocene boundary at a nearby Ross Sea site (15). Accordingly, we applied a similar approach to directly compare the timing of proximal ice volume changes during the Early Oligocene against high-resolution temperature and ice volume proxy records derived from distal deep-sea sequences.

Clast abundance (Fig. 2) reflects glacial proximity and has been shown in a previous study to be controlled by orbital forcing in conjunction with the deposition of type B cycles in the lower part of CRP-3 (16). To similarly test for the role of orbital forcing within the laterally extensive glacial advances within the type A cycle succession in the upper 300 m of the CRP-3 core, we applied a singular spectrum analysis (see supplementary materials) to the clast abundance time series and a new record of luminance, which reflects changing proportions of clay and sand in sedimentary environments controlled by the proximity to the ice margin and by changes in water depth associated with RSL fluctuations (14). An independently derived age model for CRP-3, based on biochronologic calibration of a magnetic reversal stratigraphy (16), together with identification of the orbital components in these

records enables a one-to-one correlation of sedimentary cycles to the highly resolved, orbitally tuned $\delta^{18}O$ record from the deep sea (2, 17) (Fig. 2). A key age constraint in the CRP-3 record is the precisely dated transition (±5000 years) at 31.1 Ma between magnetic polarity chrons C12n and C12r at 12.5 mbsf (13) (fig. S5).

Variation in facies and clast abundance within type B shallow-marine sedimentary cycles have previously been interpreted to reflect periodic advance and retreat of land-terminating alpine glaciers in the Transantarctic Mountains (15) in response to precession and obliquity forcing (16) (Fig. 2). This direct response to orbitally paced local insolation forcing indicates a highly dynamic AIS that advanced and retreated during the early icehouse phase of the EOGM. The first sedimentary evidence of ice advance onto the Ross Sea continental shelf coincides with the deposition of unconformity-bound, type A sedimentary cycles beginning at 32.8 Ma, and marks an abrupt transition in AIS sensitivity to orbital forcing that was paced by longer-duration eccentricity cycles (Figs. 2 and 3). This phase is also associated with climate cooling and increased physical weathering, as evidenced by a change in clay mineralogy (18). Type A cycles (Fig. 2) have been interpreted to represent cyclic alternations in both grounding-line proximity and RSL change (14). According to glacial isostatic adjustment (GIA) theory and given the ice marginal position of the CRP-3 site, any proximal ice thickness variation would have triggered crustal and geoidal deformations such that the resulting

[1]Dipartimento di Scienze Pure e Applicate, Università degli Studi di Urbino "Carlo Bo," 61029 Urbino, Italy. [2]Department of Geosciences, University of Massachusetts, Amherst, MA, USA. [3]Antarctic Research Centre, Victoria University of Wellington, Wellington, New Zealand. [4]GNS Science, P.O. Box 30368, Lower Hutt, New Zealand. [5]NIOZ Royal Netherlands Institute for Sea Research, Department of Coastal Systems, and Utrecht University, 1790 AB Den Burg, Texel, Netherlands. [6]Istituto Nazionale di Geofisica e Vulcanologia, 00143 Rome, Italy. [7]Department of Geology and Geophysics, Yale University, New Haven, CT, USA. [8]Ocean and Earth Science, University of Southampton, National Oceanography Centre, Southampton SO14 3ZH, UK. [9]Earth System Science Center, Pennsylvania State University, State College, PA, USA. [10]Museo Nazionale dell'Antartide, Università degli Studi di Siena, 53100 Siena, Italy. [11]Dipartimento di Scienze Fisiche, della Terra e dell'Ambiente, Università degli Studi di Siena, 53100 Siena, Italy. [12]Earth Sciences Department, University of California, Santa Cruz, CA 95064, USA.

*Corresponding author. E-mail: simone.galeotti@uniurb.it

Fig. 1. Location of key geographical and geological features in Southern McMurdo Sound. Boundary faults of the southern extension of Terror Rift are shown, together with the location of the CRP, MSSTS-1, and CIROS-1 drill sites.

local RSL change would be opposite in sign to eustatic trends and likely of larger amplitude (see supplementary materials). However, sedimentological evidence implies that glacial maxima and minima locally coincided with times of minimum and maximum RSL, respectively, for both type A and type B cycles (14). This implies that the GIA-induced RSL rise that was caused by the expansion and grounding of the ice sheet at the CRP-3 site was counterbalanced by a strong RSL drop as a consequence of the forebulge uplift driven by synchronous EAIS thickening. Therefore, we argue that the appearance of marine-grounded ice near the CRP-3 site was enhanced by flexural crustal uplift as the EAIS expanded, resulting in a RSL fall (>40 m) in phase with the hypothetical eustatic trend.

Both petrological and apatite fission track evidence (19) suggests that diamictites deposited as part of 400,000-year sedimentary cycles spanning ~17 to 157 mbsf (~32.0 to 31.1 Ma; Fig. 2) were derived both locally from the Mackay glacier and from the southern Transantarctic Mountains outlet glaciers during glacial overriding and downcutting. Flowlines that trend northwestward into McMurdo Sound from the Byrd, Skelton, and Mulock glaciers are implied by model simulation of the early Oligocene glacial expansion (10, 20).

According to our chronology and geological evidence for ice grounding, a marine-calving ice sheet first occurred in the western Ross Embayment at ~32.8 Ma, about 1 million years after the glacial maximum (Oi1) inferred by $\delta^{18}O$ values from marine carbonate isotope records (17) (Figs. 2 and 3). Oxygen isotope values paired with southern high-latitude Mg/Ca records (3) indicate that the AIS volume was slightly larger across Oi1a (~32.8 Ma) than across the EOGM. The Oi1a shift coincides, within the degree of uncertainty shown in Fig. 3 (see also fig. S17), with the CO_2 minimum [~600 ppm by volume (ppmv)] at the end of a ~40% decline beginning in the late Eocene (7, 21) (Fig. 3). Declining CO_2 levels that culminate during Oi1a are fully consistent with model-derived CO_2 thresholds for Antarctic glaciation (20). The Oi1a interval also corresponds to a long-term minimum in eccentricity and obliquity (22), similar to the orbital configuration favoring the onset of glaciation across Oi1 (Fig. 3), implying that an extended period of low seasonality with cooler summers contributed to these long-period glacial maxima.

Therefore, we argue that despite ice expansion during the EOGM, the nascent AIS was strongly sensitive to orbitally paced, local insolation forcing until a CO_2 threshold of ~600 ppmv was crossed at 32.8 Ma (Fig. 3 and fig. S17). After 32.8 Ma, an expanded continental-scale ice sheet displayed progressively stronger orbital ice sheet hysteresis; such behavior is also suggested by ice models (20, 23). Our observations from the CRP-3 record are also consistent with far-field ice volume proxies that indicate RSL changes of ~25 m in the time interval 33.4 to 32.8 Ma (9, 11), equivalent to ~40% of present-day AIS volume. By contrast, after 32.8 Ma, a protracted period of RSL stability is observed in $\delta^{18}O$ records, which corresponds with our proximal evidence for an AIS that was relatively insensitive to higher-frequency orbital forcing (11) until ~29 Ma, when CO_2 values again increased to >600 ppm (24) (fig. S17). Our observations of AIS history and behavior lead us to conclude that the partial pressure of atmospheric CO_2 was the primary influence on the overall climate state and variability of AIS volume, including its sensitivity to orbital forcing, which implies a close linkage between carbon cycle dynamics and AIS evolution on both long- and short-period orbital time scales. Indeed, amplification of the long-period eccentricity component—observed in the CRP-3 record at ~32 Ma—tracks the establishment of low-latitude $\delta^{13}C$ variability with a 405,000-year periodicity (25).

The general orbital coherence and phasing between glacial cycles and marine $\delta^{13}C$ records (Fig. 2) indicates that carbon cycle feedbacks
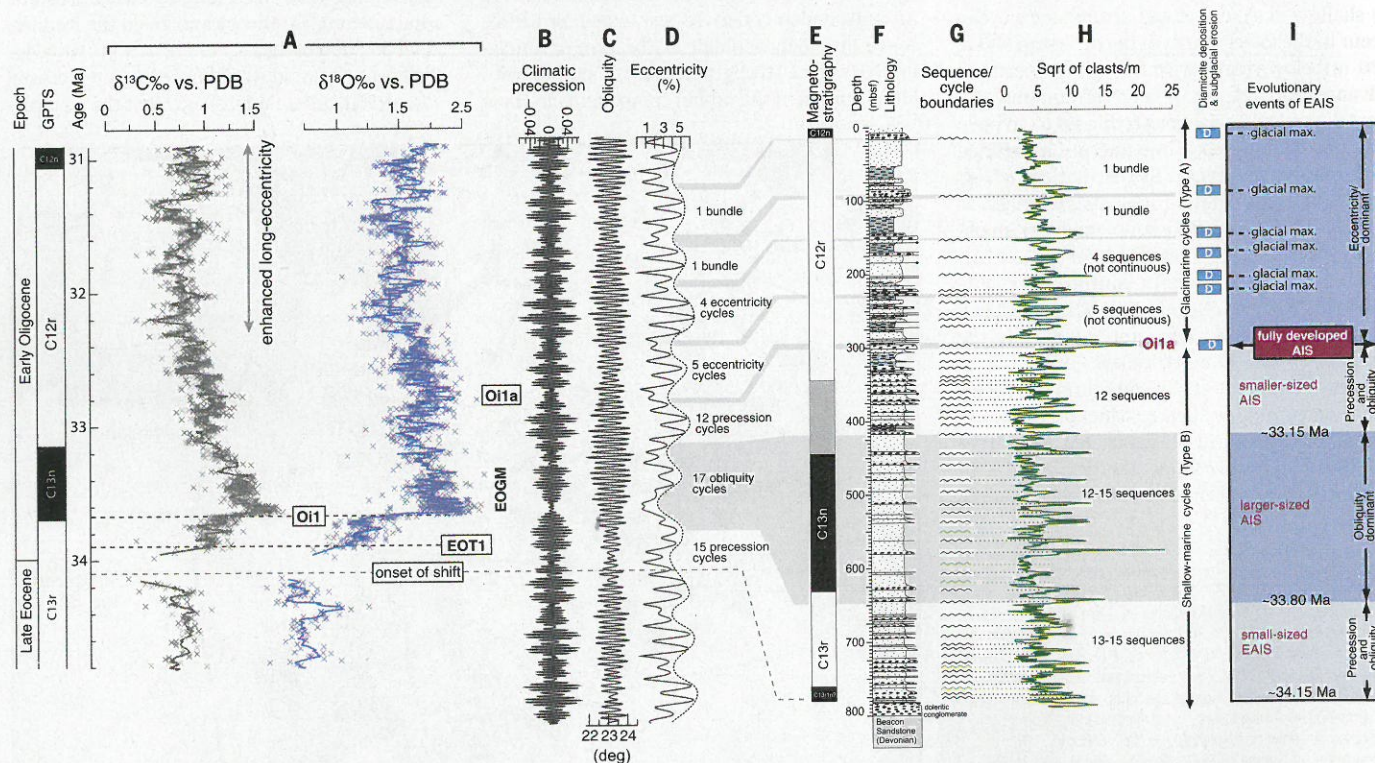
Fig. 2. Astrochronological calibration of glacial events across the Eocene-Oligocene climate transitions. (A) Deep-sea oxygen and carbon isotopic record from ODP Site 1218 (2, 17). **(B** to **H)** Time series for climatic precession (B), obliquity (C), and eccentricity (D) correlated with magnetostratigraphy (E), lithostratigraphy (F), sequence stratigraphy (G) (13, 14), and square root of clast abundance (H) (30) for the Late Eocene–Early Oligocene CRP-3 drillcore. Thirty-seven shallow-marine sedimentary cycles (sequences; type B) occur in the lower 500 m of the core record, controlled by advances and retreats of land-terminating glaciers associated with sea-level oscillations of less than 20 m. Eleven overlying glaciomarine sedimentary cycles (sequences; type A), each bounded by glacial surfaces of erosion, occur in the upper 300 m of the CRP-3 core, and record oscillations in the extent of a more expansive marine-terminating ice sheet in Ross Embayment. **(I)** Inferred stages and events in the development of the AIS across the Eocene-Oligocene boundary and their relationship to orbital forcing.
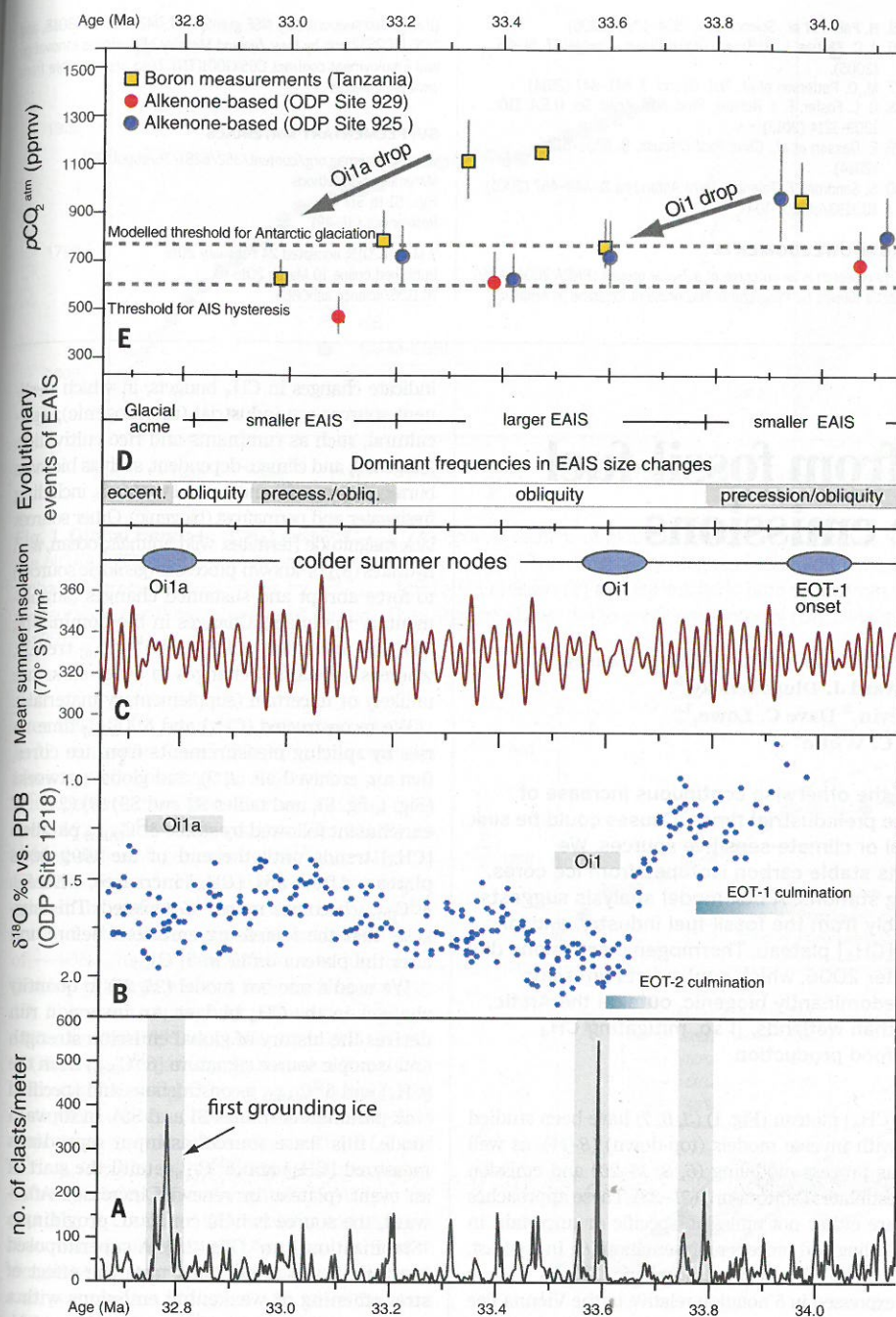
Fig. 3. Major glacial events recorded by clast abundance peaks from the CRP-3 core. (**A** and **B**) Events [gray bands in (A)] are calibrated to the astrochronologically tuned $\delta^{18}O$ record from ODP Site 1218 (B) (*2*). (**C**) Major peaks in clast abundance from CRP-3 correspond to the onset of the EOT-1 shift and glacial maxima at the Oi1 and Oi1a, and are associated with prolonged intervals characterized by cold southern high latitude summers as expressed in the 70°S mean summer insolation. (**D**) AIS volume changes recorded by the sedimentary sequences and clast abundance (see Fig. 2) are paced by the influence of obliquity and precession on a smaller-sized terrestrial ice sheet between 34.2 and 32.8 Ma. (**E**) Comparison with available atmospheric pCO_2 (partial pressure of atmospheric CO_2) records based on boron isotope (*21*) and alkenone (*7*) proxies shows that the earliest evidence of ice sheet grounding in the CRP-3 core occurs at the Oi1a event (32.9 to 32.8 Ma), coincident with a major peak in clast abundance and a longer-term drop in atmospheric CO_2 to below ~600 ppm.

contributed to CO_2 changes and amplification of short- and long-period eccentricity-paced glacial-interglacial cycles in the Early Oligocene (*26*), similar to the climate-carbon cycle dynamics associated with Northern Hemisphere glacial cycles during the Pleistocene. Coupled global climate–ice sheet models predict that the AIS should display threshold-like behavior in response to long-term trends in atmospheric CO_2 levels (*20*). For example, the stability threshold for marine-based sectors of the AIS has been shown to be ~400 ppm; between 300 and 400 ppm, marine ice sheets are highly dynamic in response to orbital forcing (*27, 28*). Intermodel comparisons suggest a larger range of atmospheric CO_2 values (~560 to 920 ppm) for AIS glaciation (*29*). Data presented in our study imply that a CO_2 threshold for a continental-scale Antarctic ice sheet occurred at ~600 ppm, and that AIS sensitivity to insolation forcing and vulnerability to melt can be expected to increase markedly between 600 and 750 ppm.

REFERENCES AND NOTES

1. J. C. Zachos, T. M. Quinn, K. A. Salamy, *Paleoceanography* **11**, 251–266 (1996).
2. H. K. Coxall, P. A. Wilson, H. Pälike, C. H. Lear, J. Backman, *Nature* **433**, 53–57 (2005).
3. S. M. Bohaty, J. C. Zachos, M. L. Delaney, *Earth Planet. Sci. Lett.* **317–318**, 251–261 (2012).
4. C. H. Lear, T. R. Bailey, P. N. Pearson, H. K. Coxall, Y. Rosenthal, *Geology* **36**, 251 (2008).
5. Z. Liu, S. Tuo, Q. Zhao, X. Cheng, W. Huang, *Chin. Sci. Bull.* **49**, 2190–2197 (2004).
6. Z. Liu *et al.*, *Science* **323**, 1187–1190 (2009).
7. M. Pagani, J. C. Zachos, K. H. Freeman, B. Tipple, S. Bohaty, *Science* **309**, 600–603 (2005).
8. K. G. Miller *et al.*, *Bull. Geol. Soc. Am.* **120**, 34–53 (2008).
9. M. E. Katz *et al.*, *Nat. Geosci.* **1**, 329–334 (2008).
10. D. S. Wilson, D. Pollard, R. M. DeConto, S. S. R. Jamieson, B. P. Luyendyk, *Geophys. Res. Lett.* **40**, 4305–4309 (2013).
11. K. G. Miller *et al.*, *Science* **310**, 1293–1298 (2005).
12. K. Billups, D. P. Schrag, *Earth Planet. Sci. Lett.* **209**, 181–195 (2003).
13. F. Florindo, G. S. Wilson, A. P. Roberts, L. Sagnotti, K. L. Verosub, *Global Planet. Change* **45**, 207–236 (2005).
14. C. R. Fielding, T. R. Naish, K. J. Woolfe, *Terra Antarctica* **8**, 217–224 (2001).
15. T. R. Naish *et al.*, *Nature* **413**, 719–723 (2001).

16. S. Galeotti et al., Palaeogeogr. Palaeoclimatol. Palaeoecol. 335–336, 84–94 (2012).
17. H. K. Coxall, P. A. Wilson, Paleoceanography 26, PA2221 (2011).
18. W. Ehrmann, M. Setti, L. Marinoni, Palaeogeogr. Palaeoclimatol. Palaeoecol. 229, 187–211 (2005).
19. V. Olivetti, M. L. Balestrieri, F. Rossetti, F. M. Talarico, Tectonophysics 594, 80–90 (2013).
20. R. M. DeConto, D. Pollard, Nature 421, 245–249 (2003).
21. P. N. Pearson, G. L. Foster, B. S. Wade, Nature 461, 1110–1113 (2009).
22. J. Laskar et al., Astron. Astrophys. 428, 261–285 (2004).
23. D. Pollard, R. M. DeConto, Global Planet. Change 45, 9–21 (2005).
24. Y. G. Zhang, M. Pagani, Z. H. Liu, S. M. Bohaty, R. DeConto, Philos. Trans. R. Soc. A 371, 20130096 (2013).
25. H. Pälike et al., Science 314, 1894–1898 (2006).
26. J. C. Zachos, L. R. Kump, Global Planet. Change 47, 51–66 (2005).
27. M. O. Patterson et al., Nat. Geosci. 7, 841–847 (2014).
28. G. L. Foster, E. J. Rohling, Proc. Natl. Acad. Sci. U.S.A. 110, 1209–1214 (2013).
29. E. Gasson et al., Clim. Past Discuss. 9, 5701–5925 (2014).
30. S. Sandroni, F. Talarico, Terra Antartica 8, 449–467 (2001). 10.3133/of2007-1047

ATMOSPHERIC METHANE

A 21st-century shift from fossil-fuel to biogenic methane emissions indicated by $^{13}CH_4$

Hinrich Schaefer,[1]* Sara E. Mikaloff Fletcher,[1] Cordelia Veidt,[2] Keith R. Lassey,[1]†
Gordon W. Brailsford,[1] Tony M. Bromley,[1] Edward J. Dlugokencky,[3]
Sylvia E. Michel,[4] John B. Miller,[3] Ingeborg Levin,[2] Dave C. Lowe,[1]‡
Ross J. Martin,[1] Bruce H. Vaughn,[4] James W. C. White[4]

Between 1999 and 2006, a plateau interrupted the otherwise continuous increase of atmospheric methane concentration [CH_4] since preindustrial times. Causes could be sink variability or a temporary reduction in industrial or climate-sensitive sources. We reconstructed the global history of [CH_4] and its stable carbon isotopes from ice cores, archived air, and a global network of monitoring stations. A box-model analysis suggests that diminishing thermogenic emissions, probably from the fossil-fuel industry, and/or variations in the hydroxyl CH_4 sink caused the [CH_4] plateau. Thermogenic emissions did not resume to cause the renewed [CH_4] rise after 2006, which contradicts emission inventories. Post-2006 source increases are predominantly biogenic, outside the Arctic, and arguably more consistent with agriculture than wetlands. If so, mitigating CH_4 emissions must be balanced with the need for food production.

Anthropogenic CH_4 emissions have almost tripled [CH_4] since preindustrial times (1–3). This contributes strongly to anthropogenic climate change through radiative forcing and impacts on atmospheric chemistry, particularly hydroxyl consumption, tropospheric ozone generation, and water vapor formation in the stratosphere (4). In a positive feedback to climate change, natural sources such as CH_4 hydrates, tundra, and permafrost may increase (5). We must therefore understand how the CH_4 budget responds to human activities and environmental change. The onset and end of the 1999–2006

[CH_4] plateau (Fig. 1) (3, 6, 7) have been studied with inverse models (top-down) (8–14), as well as process modeling (6, 8, 15–20) and emission estimates (bottom-up) (21–23). These approaches are either not emission-specific or uncertain in scaling and process representation (8). In contrast, the $^{13}C/^{12}C$ ratio in atmospheric CH_4 [$\delta^{13}C_{(Atm)}$; expressed in δ notation relative to the Vienna Pee Dee Belemnite standard] is controlled by the relative contributions from source types with distinctive isotope signatures $\delta^{13}C_{(So)}$ [biogenic ~–60 per mil (‰), such as wetlands, agriculture, and waste; thermogenic ~–37‰, such as fossil-fuels; pyrogenic ~–22‰, such as biomass burning] (3, 24). Large and overlapping ranges for $\delta^{13}C_{(So)}$ in field studies of the main source types and even individual sources (such as wetlands) (24) average out at the global scale so that $\delta^{13}C_{(So)}$ is suitable to characterize emissions. Sink processes with characteristic isotopic fractionation ε (25) [for example, hydroxyl (OH) $\varepsilon = -3.9‰$; chlorine in the marine boundary layer (Cl-MBL) $\varepsilon = -60‰$; stratospheric loss $\varepsilon = -3‰$; or oxidation by soils $\varepsilon = -20‰$] (table S1) (26, 27) also influence $\delta^{13}C_{(Atm)}$. Therefore, $\delta^{13}C_{(Atm)}$ variations

indicate changes in CH_4 budgets, in which pertinent sources are industrial (thermogenic); agricultural, such as ruminants and rice cultivation (biogenic); and climate-dependent, such as biomass burning (pyrogenic) and natural wetlands, including freshwater and permafrost (biogenic). Other sources lack magnitude [termites, wild animals, ocean, and hydrates (8)] or known processes (geologic sources) to force abrupt and sustained changes (supplementary materials). Changes in the dominating OH sink may affect [CH_4] and $\delta^{13}C_{(Atm)}$ trends, whereas substantial changes in other sinks are unlikely or uncertain (supplementary materials).

We reconstructed [CH_4] and $\delta^{13}C_{(Atm)}$ time series by splicing measurements from ice cores, firn air, archived air (1, 2), and global networks (Fig. 1, fig. S1, and tables S2 and S3) (3) (25). ^{13}C enrichment followed by stable $\delta^{13}C_{(Atm)}$ parallels [CH_4] trends until the end of the 1999–2006 plateau. Afterward, [CH_4] increases, whereas $\delta^{13}C_{(Atm)}$ becomes more ^{13}C-depleted. This suggests that the increasing emissions before and after the plateau differ in $\delta^{13}C_{(So)}$.

We used a one-box model (25, 27) to quantify changes in the CH_4 budget. An inversion run derives the history of global emission strength and isotopic source signature [$\delta^{13}C_{(So)}$] from the [CH_4] and $\delta^{13}C_{(Atm)}$ reconstructions and specified sink parameters (tables S1 and S3). In forward mode, this "base source" as input reproduces measured [CH_4] and $\delta^{13}C_{(Atm)}$ until the start of an event (plateau or renewed increase). Afterward, the source is held constant, providing a "Stabilization Run" (Fig. 2A). A superimposed "perturbation source" then tests the effect of strengthening or weakening emissions with a prescribed perturbation $\delta^{13}C_{(So)}$ on $\delta^{13}C_{(Atm)}$. Alternatively, sink variability can be implemented for equivalent tests. The modeling design is detailed in section 1.3 of (25).

Stabilization Run 92 (SR92) tests whether emissions simply stabilized to cause the [CH_4] plateau (assuming constant sinks) (28). The base source is run from 1700 to 1992, during which time emission rates show steady trends (fig. S2); afterward, emissions are held constant at 1991–1992 rates and average 1982–1992 $\delta^{13}C_{(So)}$. These choices remove disruptions by the Mount Pinatubo eruption (supplementary materials). Model-data mismatches after the plateau onset (Fig. 2) suggest a changing source mix and emission reductions. The latter occur abruptly after 1992, for an average 7.2 to 11.2 Tg loss in annual global emissions

[1]Climate and Atmosphere Center, National Institute of Water and Atmospheric Research (NIWA), 301 Evans Bay Parade, Wellington 6021, New Zealand. [2]Institut für Umweltphysik, Heidelberg University, Im Neuenheimer Feld 229, 69120 Heidelberg, Germany. [3]National Oceanic and Atmospheric Administration (NOAA), Earth System Research Laboratory (ESRL), Global Monitoring Division, 325 Broadway, Boulder, CO 80305, USA. [4]Institute of Arctic and Alpine Research (INSTAAR), University of Colorado, Boulder, CO 80309, USA.
*Corresponding author. E-mail: hinrich.schaefer@niwa.co.nz
†Present address: Lassey Research & Education, 4 Witako Street, Lower Hutt 5011, New Zealand. ‡Present address: LoweNZ, 31 Queen Street, Lower Hutt 5012, New Zealand.